1

Diamondized carbon nanoarchitectures as electrocatalytic material for sulfate-based

oxidizing species electrogeneration

Karla Caroline de Freitas Araújo[1], Elisama Vieira dos Santos[1], Mattia Pierpaoli[2],

Mateusz Ficek[2], José Eudes L. Santos[1], Carlos A. Martínez-Huitle[1,*] Robert

Bogdanowicz[2,*]

[1]Instituto de Química, Universidade Federal do Rio Grande do Norte, Natal, Rio Grande do Norte, Brazil.

[2]Faculty of Electronics, Telecommunications and Informatics, Gdańsk University of Technology, 11/12 G. Narutowicza St, 80-233 Gdańsk, Poland

*Corresponding author's e-mail:

carlosmh@quimica.ufrn.br (C.A. Martínez-Huitle),

rbogdan@eti.pg,edu.pl (Robert Bogdanowicz)

Abstract

The introduction of nanotechnology seems to be an imperative factor to intensify the synergic effects of electrocatalytic materials to produce strong oxidant species or to increase the active sites on their surfaces as well as to enhance the conversion yield in a fuel cell, high-added value products, electrolytic treatment for environmental protection or the detection limit in electroanalysis. Recently, a new type of 3D-diamond electrodes was developed with boron-doped carbon nanowalls (B:CNW), which was manufactured using the microwave plasma-assisted chemical vapor deposition (CVD) process, improving the charge transfer and enhancing the electrochemical performance. The applicability of a BDD/boron-doped carbon nanowalls (BDD/B:CNW) anodes to degrade organic pollutants has been already investigated; however, no attempts at the electrosynthesis of oxidizing species using these diamond-carbon nanostructures have been reported yet. Therefore, the electrosynthesis of sulfate-based oxidizing species was studied here to answer relevant questions from both fundamental and practical point-of-view. The results demonstrated that persulfate was efficiently produced at the BBD plate, while that the ion-radical sulfate could be the most important oxidant at BDD/B:CNW anode when compared to other electrocatalytic materials, including BDD surfaces. Persulfate concentrations ranged from 3 to 6 μM, depending on the applied current density (2.5, 5.0, and 15 mA cm^{-2}), at diamond electrodes. A dye-model pollutant - methyl orange (MO) was degraded below the limit of detection within 45 min using BDD/B:CNW when *in-situ* sulfate-based oxidizing species were electrogenerated. These kinds of 3D-diamond-carbon nanostructures are thus promising as novel electrocatalyst for various catalytic applications in the environmental and energy fields.
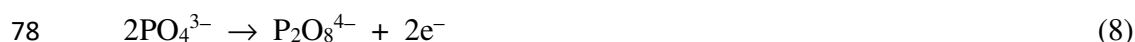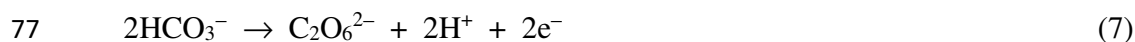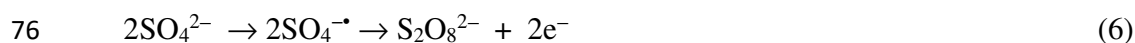
2

49   *Keywords*: boron-doped diamond electrode, sulfate-based oxidizing species, diamond-

50   carbon nanoarchitectures, electrocatalyst, electrogeneration.

1. Introduction

The scientific community has shown a preference to apply EO as an environment-friendly electrochemical process because of its uncomplicatedness and acceptance among the electrochemical advanced oxidation processes (EAOPs), in terms of electrolytic technology, amenability, environmental compatibility, automation, no reagents use, renewable energies-driven and in-situ production of higher concentration of oxidants [1]. In the last decades, EO has competently demonstrated its effectiveness to mineralize different organic compounds in a great variety of water matrices or wastewaters [2]. Nevertheless, the extension of mineralization/degradation of these pollutants and their concentration as well as the type of the electrogenerated oxidants strongly depends on the operating parameters and the nature of the anode electrocatalytic material [3,4].

Various electrodes have been used in EO, like Ir-, Pt-, Ru-, Ti-, Pb- and Sn- oxide-based anodes as well as synthetic diamond films [5,6]. However, boron-doped diamond (BDD) anodes are considered the most effective electrocatalytic materials for degrading/mineralizing refractory/priority pollutants and waterborne agents [1,2,7–9]. It is due to their effective *in-situ* production of oxidizing agents, at higher concentrations, mainly reactive oxygen species (ROS) (Eq. (1)-(5)) [9]. Also, peroxodisulfate ($S_2O_8^{2-}$), peroxodicarbonate ($C_2O_6^{2-}$) and peroxodiphosphate ($P_2O_8^{4-}$) can be electrochemically formed with ROS from the oxidation of sulfate or bisulfate by Eq. (6), bicarbonate by Eq. (7) and phosphate by Eq. (8) at the BDD surface [10,11].

$$BDD + H_2O \rightarrow BDD(^{\bullet}OH) + H^+ + e^- \tag{1}$$

$$^{\bullet}OH \rightarrow {^{\bullet}O} + H^+ + e^- \tag{2}$$

$$2{^{\bullet}O} \rightarrow O_2 \tag{3}$$

4

74 $\quad 2^{\bullet}OH \rightarrow H_2O_2$ $\hfill$ (4)

75 $\quad O_2 + {}^{\bullet}O \rightarrow O_3$ $\hfill$ (5)

76 $\quad 2SO_4{}^{2-} \rightarrow 2SO_4{}^{-\bullet} \rightarrow S_2O_8{}^{2-} + 2e^-$ $\hfill$ (6)

77 $\quad 2HCO_3{}^- \rightarrow C_2O_6{}^{2-} + 2H^+ + 2e^-$ $\hfill$ (7)

78 $\quad 2PO_4{}^{3-} \rightarrow P_2O_8{}^{4-} + 2e^-$ $\hfill$ (8)

79 As already scientifically stated, the effective electrosynthesis of oxidizing species requires

80 an electrode with a large surface area, high electrocatalytic activities, long-term stability, as

81 well as a low cost of materials [5,12]. Thus, the introduction of nanoarchitectures seems to

82 be an essential factor to intensify the synergic effects of electrocatalytic materials to produce

83 strong oxidant species or to increase the active sites on their surfaces [13]. Novel

84 nanostructured materials can exhibit better electrochemical properties than their bulk

85 counterparts with a specific pore dimension distribution and well-defined structure-

86 morphology, maximizing the exposed-surface area and minimizing the mass transport

87 phenomena [14–16]. Thus, the advances in the preparation of highly sophisticated

88 electrocatalytic nanomaterials may lead to further improvements in the mineralization of

89 organic pollutants as well as the electrosynthesis of oxidants, making them suitable for smart

90 water solutions [17]. These technologies will play a key role in achieving the Sustainable

91 Development Goal 6 (SDG6) since these represent a substantial opportunity if their

92 implementation is carried out to guarantee sustainability and increase competence in water

93 management (to treat and distribute water for human use) [18].

94 Recently, a versatile electrode was discovered, called the "3D-nanostructured BDD/B:CNW"

95 anode. This 3D-diamondized-carbon nanostructure possesses extraordinary electrochemical

96 properties (e.g., peculiar morphology, specific surface area and the larger extends of exposed

97 edges with a greater number of functional groups and chemisorbed heteroatoms, in particular,

98 oxygen), allowing a higher reactivity of the carbonaceous nanostructure for environmental,

99 fuel and sensors applications, compared to 2D-BDD electrode [19–21]. However, no

100 information concerning the effectiveness of this 3D-nanostructured BDD/B:CNW anode to

101 electrogeneration oxidants has been reported yet. Thus, for the first time, the electrosynthesis

102 of sulfate-based oxidants species has been studied by using a 3D-nanoarchitectured

103 BDD/B:CNW anode to answer relevant questions from both fundamental and practical point-

104 of-view. An organic model compound was also chosen to prove the oxidative efficiency of

105 *in-situ* $S_2O_8^{2-}$ electrogeneration when compared with other electrode materials. The results

106 are discussed considering the existing literature on nanostructured electrodes for

107 electrocatalytic advanced oxidation processes.

108

109 **2. Materials and Methods**

110 **2.1. Materials**

111 All reagents were of analytical grade and used without further purification. The water was

112 obtained from purified water (Milli-Q system, with resistivity ≥18 MΩ cm at 25 °C). Methyl

113 orange (MO) purity was 95% and it was used as received.

114

115 **2.2. Synthesis and characterization of BDD/B:CNW**

116 BDD and BDD/BCNW were synthesized using the MWPECVD system (SEKI Technotron

117 AX5400S, Japan). Thin films were grown on niobium substrates for a total of 5 h, resulting

118 in 3 µm of thickness. The detailed parameters of the thin film synthesis can be found

119 elsewhere, for BDD [ref1] and for the BDD:BCNW in Pierpaoli et al [ref2, ref3]~~BCNW in~~

120 ~~Siuzdak *et al.* [22], Dettlaff *et al.* [23], and Sobaszek *et al.* [24]~~ . The surface characteristics

6

121 of the BDD/B:CNW was carried out using a Hitachi model TM 3000 top microscope with a

122 high sensitivity semiconductor backscattered electron detector to obtain scanning electron

123 microscopy (SEM) images, using a significant magnification and operating at 15 kV voltage

124 acceleration with a tungsten filament. The SEM images were taken under a vacuum at

125 controlled temperatures and the energy dispersive X-ray (EDS) spectrum was obtained to

126 analyze the concentrations of the elements in the diamond-carbon nanostructures. Raman

127 spectra were recorded in the 50–3200 cm^{-1} range, upon excitation by a 532 nm laser; the

128 spectral resolution was equal to 2.9 cm^{-1}, in the range of 50–2000 cm^{-1} and 2.4 cm^{-1} in the

129 range of 2000–3200 cm^{-1} with an integration time of 5 s (20 averages), with a diffraction

130 grating of 300 lines/mm^2.

131 **2.3.   Electrochemical measurements**

132   Experiments were carried out in a conventional three-electrode system in Pyrex material

133 with a capacity of 10 mL, and measurements were performed between 0.0 and +1.8 V at 10

134 mV s^{-1} for quasi-steady polarization curves in 0.05 M of Na_2SO_4. BDD and BDD/B:CNW

135 anodes have significant areas in cm^2, however, an exposed geometric area of ca. 0.075 cm^2

136 was used as the working electrode for electrochemical measurements, while this area was

137 increased for bulk electrolysis (see next subsection). A platinum wire and an Ag/AgCl (3 M)

138 were employed as the auxiliary and reference electrodes, respectively. The electroactive

139 surface area (A_{real}) and the differential capacitance (C_{DL}) were experimentally estimated [25–

140 27], according to Eq. 1. To do that, a potential range was selected, for BDD and BDD/B:CNW

141 electrodes, where a non-Faradaic current response is registered. This range was ≈0.2 V

142 potential window centered on the open-circuit potential of the system. Then, cyclic

143 voltammetry (CV) measurements were conducted in static solution by sweeping the potential

144 across the non-Faradaic region and back at 9 different scan rates (0.02, 0.04, 0.06, 0.08, 0.10,

145 0.12, 0.14, 0.16, 0.18 and 0.20 V s^{-1}) at 25±1°C in 0.05 M of Na_2SO_4. For each measurement,

146 five voltammetric profiles were recorded, and the last curve was always selected to be used for

147 plotting the graphics in this work.

$$148 \qquad A_{real} = \frac{C_{DL}}{C^*} = \frac{\mu F}{\frac{\mu F}{real\ cm^2}} = cm^2 \qquad (1)$$

149 In Eq. 1, C_{DL} is the differential capacitance of the electrode-electrolyte interface and C^* is

150 approximately 60 µF (real cm^2)$^{-1}$ which is a reference value for porous materials, regardless of

151 its composition [25,27]. Experiments were performed with an Autolab

152 potentiostat/galvanostat model PGSTAT302N.

153

154 ### 2.4. Spectrophotometric analysis

155 For UV-vis spectrophotometric measurements to determine the production of persulfate, a

156 Shimadzu spectrophotometer model 1800 was employed by using *in-situ* chemical oxidation

157 (ISCO) method [28,29], operating from 190 to 800 nm. A single quartz cuvette was used

158 with an optical path of 1 cm. It is important to remark that persulfate generation can be

159 followed by ISCO method without H_2O_2 interference because the analysis of absorption

160 spectra of a yellow color solution resulting from the reaction of persulfate and iodide in the

161 presence of sodium bicarbonate reveals a clear absorbance spectrum at 352 nm.

162

163 ### 2.5. Electrochemical determination of methyl orange concentration

164 Electroanalytical measurements were carried out in a conventional three-electrode system in

165 Pyrex material with a capacity of 25 mL for determining MO concentrations by differential

166 pulse voltammetry (DPV) analysis. BDD anode (silicon substrate, 500 ppm of boron doping,

8

167 2-3 μm of thickness), with an exposed geometric area of 0.28 cm^2, was used as the working

168 electrode, while a platinum wire and Ag/AgCl (KCl 3 M) were employed as the auxiliary

169 and reference electrodes, respectively. DPV experiments were performed with an Autolab

170 PGSTAT 320N model to establish an analytical curve by measuring different concentrations

171 of MO in 0.05 M Na$_2$SO$_4$. Other details of the procedure are as follows: equilibration time,

172 5 s; modulation time, 0.05 s; interval time, 0.5 s; initial potential, 0 V; end potential, +1.8 V;

173 step potential, 25 mV; and modulation amplitude, 100 mV. For determining MO

174 concentration at each predetermined time during EO tests, the samples were spiked with a

175 known quantity of a standard solution, and the standard addition method was implemented.

176

177 ### 2.6. Bulk experiments

178 Experiments were carried out using a bulk electrochemical cell under stirring agitation which

179 consisted of several electrodes (anodes such as BDD plate, BDD/B:CNW, TiPt, Pb/PbO$_2$,

180 Ti/TiO$_2$-nanotubes/PbO$_2$ and Ti as cathode, respectively) of 1.5 cm of diameter (geometrical

181 area $\approx$7.07 cm^2). Electrolysis of 50 mL of a synthetic solution containing 0.05 M Na$_2$SO$_4$ as

182 the supporting electrolyte was performed by applying 2.5, 10, and 15 mA cm^{-2} for 150 min

183 to prepare sulfate-based oxidizing species. Sulfate concentration was chosen based on the

184 existing literature to produce a significant concentration of persulfate [29,30]. During all

185 experiments, samples of the sulfate-based oxidizing solutions were collected at the end of the

186 electrolysis, and subsequently, these were analyzed by the ISCO-spectrophotometric method,

187 determining the final sulfate-based oxidants concentration produced. For the EO of an

188 organic target compound, 25 mL of 0.05 M of Na$_2$SO$_4$ containing 10 mg L^{-1} of MO were

189 electrochemically treated by mixing with magnetic stirring for 40 min and aliquots were

9

190   withdrawn at predetermined times to determine chemical oxygen demand (COD) and the

191   concentration of the target pollutant by the electroanalytic procedure. COD levels were

192   measured by using pre-dosed reagents (HANNA® vials) in 2 mL samples. Samples for COD

193   determination were digested in a thermal reactor (HANNA instrument) at 150°C for 2 h.

194   Subsequently, the samples initial and final, for all oxidation tests, were analyzed on a

195   spectrophotometer (Hanna HI 83099), at 25°C.

196

197   **3. Results and Discussion**

198   **3.1. Characterization of diamond electrode**

199   The BDD/B:CNW electrode morphology presents microscale valleys with a diameter of a

200   few micrometers, as observed in the SEM images (Fig. 1a). As previously reported [13,14,31]

201   and confirmed by SEM images; on the one hand, carbon grows vertically in form of multi-

202   layer graphene walls covered by diamond clusters. Microcavities having an opening in the

203   range between tens and hundreds of nanometres are formed between the nanowall boundaries

204   (Fig. 1a). On the other hand, "nano-flaps" also grow perpendicularly as secondary

205   protuberances to the surface of the nanowalls due to the process of synthesis [13,14,31].

206   Meanwhile, EDS spectrum evidence that the concentrations of the elements in the diamond-

207   carbon nanostructures are preferentially carbon and oxygen, confirming the BDD/B:CNW

208   composition (Fig. 1b).

209   In this context, the CVD process developed by Bogdanowicz's group [14] is an innovative

210   approach to obtaining a carbon nanostructure with concave and convex curvatures in a simple

211   way [13,14,31]. Thus, it was possible to understand that the electrode surface and their

212   composition, as well as the density of electronic states of electrode materials [XXX], could

213   influence during the production of oxidant species. From the Raman spectra (Fig. 1c), the

10

intense peak at 1332 cm−1 sharply observed for the BDD sample is assigned to sp3-hybridized carbon, which decreases in intensity and downshift to 1310 cm-1 for the BDD:BCNW sample, which is typical for typical for heavily boron-doped diamond [ref], since the diborance concentration inside the reactor increases as well. Moreover, it is possible to observe the G-band at around 1580 cm−1, arising from the presence of graphitic material (i.e., sp2-C), and the D-band which indicates defects in graphitic structures. Finally, D' is another second-order Raman band, appearing as a shoulder peak of the G band, originating from a second-order Raman scattering at the K point, involving one iTO phonon and one defect state [ref].
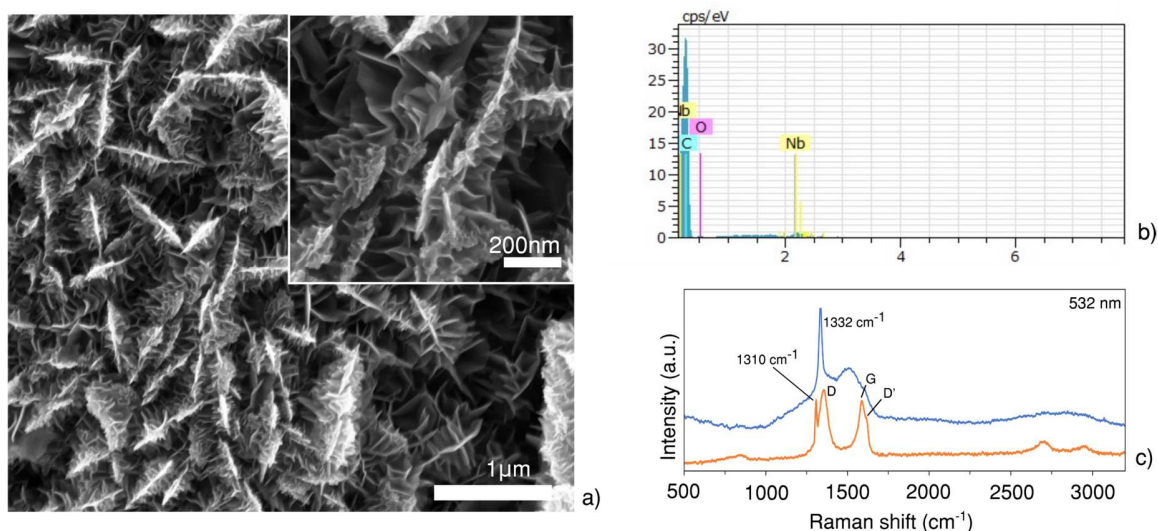

Fig. 1. (a) SEM images of the BDD/BCNW grown on Nb, (b) EDS spectrum, confirming the composition of BDD/BCNW electrode: C (94.42 wt.%, 97.40 at.%), O (2.90 wt.%, 2.25 at.%) and Nb (2.68 wt.%, 0.36 at.%). And (c) Raman spectra for the BDD and BDD:BCNW samples.

3.2. Electrochemical measurements

11

231 CV curves in a non-faradaic potential range were recorded at different scan rates (0.04, 0.06,

232 0.08, 0.10, 0.12, 0.14, 0.16, 0.18 and 0.20 V s^{-1}) to estimate the electro-active surface of BDD

233 and BDD/B:CNW electrodes. By plotting the current, which was measured in the middle of

234 the double-layer region and recorded at different scan rates, versus the scan rate (e.g.:

235 BDD/B:CNW, Fig. 2); a straight line was obtained, which allowed determining the double

236 layer capacitance values for these electrocatalytic materials (Insets in Fig. 2). Then, by using

237 the Eq. (1), the geometric area of the electrodes ($\approx$0.075 cm^2) and the C_{DL} values obtained

238 (5.40 µF and 41.52 µF for BDD and BDD/B:CNW, respectively); the real surface areas were

239 estimated, obtaining 0.216 cm^2 and 0.692 cm^2 for BDD and BDD/B:CNW, respectively. It

240 is important to remark that, based on existing literature data [26], reference values (C*) for

241 compact and porous materials should be considered to estimate the electroactive surface area,

242 regardless of its composition. Then, 60 µF (real cm^2)$^{-1}$ was the reference value for

243 BDD/B:CNW, while, 25 µF (real cm^2)$^{-1}$ for BDD plate due to the most homogeneous surface

244 [26,27,32].
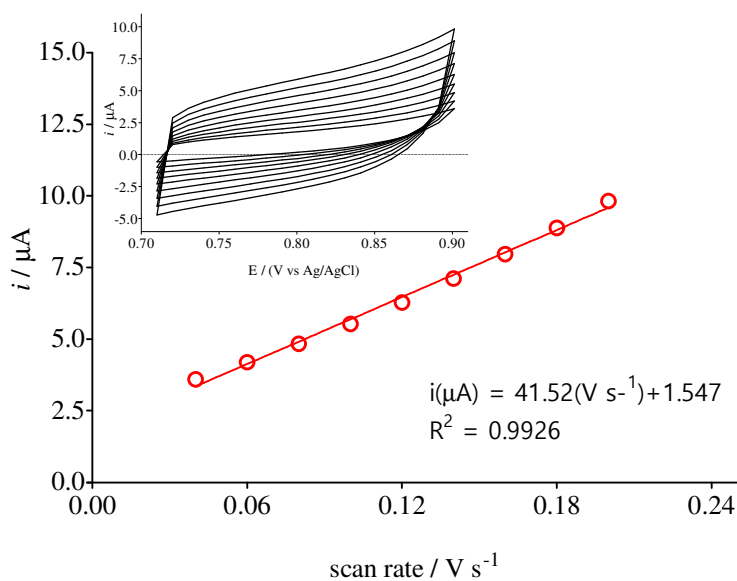
245

246 **Fig. 2.** Cyclic voltammetric (CV) analysis (from 0.04 to 0.20 V s^{-1}) to estimate the

247 capacitance for BDD/B:CNW electrode in 0.05 M of Na$_2$SO$_4$ by plotting the current values

248 in the double-layer regions as a function of scan rate. Inset: double-layer capacitance

249 measurements by using CV technique at different scan rates.

250

251 Although there are several methods to experimentally determine the real surface area such as

252 hydrogen adsorption, double layer capacitance, surface oxide reduction, underpotential

253 deposition of metals, and adsorbed carbon monoxide stripping [27]; for the case of BDD

254 electrodes, some approaches could be efficiently applied. However, the double-layer

255 capacitance method allows to obtain accurate surface measurements, avoiding significant

256 surface changes due to the oxygen/hydrogen evolution, formation/reduction of oxides, and

257 modification of carbon materials [27,32,33]. The double-layer capacitance also allows

258 measuring the total surface area accessible to the solution, and it is not destructive [27]. In

259 fact, in this case, the real electrode areas are superior to the geometrical value; it could be

260 due to the character of diamond surfaces, allowing for proper contact of the solution with all

261 active sites and consequently, a significant increase in the real area was achieved respect to

262 0.075 cm^2.

263 For BDD/B:CNW electrode, an increase in the porous properties of the material was achieved

264 due to the 3D nanostructures (see SEM images, Fig. 1) [20,21,24]; for this reason, an increase

265 in the solution contact (solution diffusion between/into the porous) could be expected [14].

266 Meanwhile, this behavior is reduced in the BDD plate due to the homogeneous surface. In

267 this context, the roughness factor (RF = A$_{real}$/A$_{geometric}$) was also determined for BDD and

268   BDD/B:CNW electrodes, considering the geometric surface and the estimated electroactive

269   area for each one of the electrodes, achieving values of about 2.88 and 9.22, respectively.

270   From these results, it is possible to deduce that, the new type of 3D-diamond electrodes with

271   boron-doped carbon nanowalls (B:CNW) increased its roughness by about 3.2-folds in

272   comparison to the BDD plate surface [14,15,21,34,35]. This result evidenced that, the

273   roughness controls the contact of the active sites with the solution and thus, increasing its

274   active area [14,21].

275   On the other hand, it is important to characterize the potential window and anodic

276   oxygen evolution reaction by electrochemical measurements at both carbon materials. Fig. 3

277   shows the polarization curves registered at BDD and BDD/B:CNW anodes in a sulfate

278   solution. A slight variation in the potential window is achieved, evidencing an important

279   change in the potential of the oxygen evolution reaction (OER). This behavior is mainly

280   associated with the different carbon constituents on the BDD surfaces as well as the

281   electrochemical decomposition of the supporting electrolyte [30,36,37]. Linear polarization

282   curves for BDD/B:CNW electrode showed that the potential for the OER was shifted to a less

283   positive potential ($\approx$1.43 V vs Ag/AgCl). Based on previous works [36,38], it was

284   demonstrated that graphite electrode presents lower oxygen overpotential than BDD

285   electrodes, similar to the behavior achieved at BDD/B:CNW. Conversely, BDD plate showed

286   to be a poor electrocatalyst for OER, shifting this reaction to more positive potentials (Fig.

287   3).
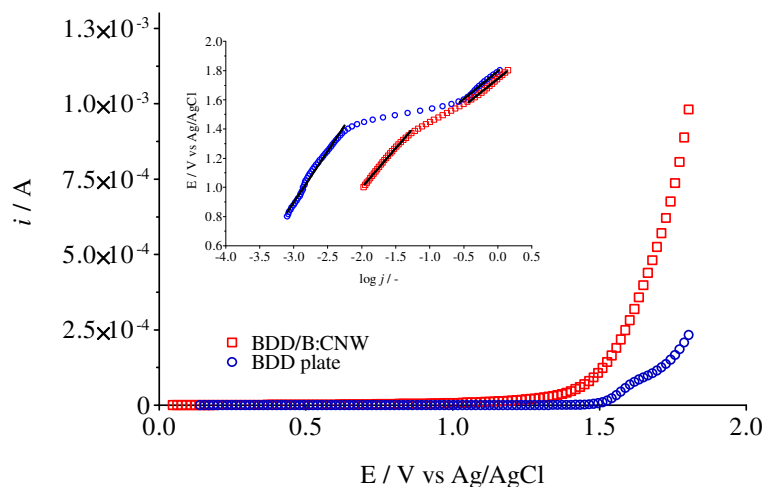
288

289   **Fig. 3.** Polarization curves registered at BDD and BDD/B:CNW electrodes in 0.05 M of

290   Na_2SO_4. Inset: data in terms of Tafel plots at lower and higher overpotential regions from the

291   potential of hydroxyl radicals' formation.

292

293   Meanwhile, additional effects could be observed when the analysis of the Tafel plots

294   is executed. E/log j plots at both BDD electrodes are shown in the inset of Fig. 3, considering

295   the real surface area for each one of them. As can be observed, the Tafel plots change their

296   slope according to the lower overpotential region (<1.6 V) or high overpotential region

297   (>1.62 V). At BDD/B:CNW, the OER seems to be the main process than that registered at

298   BDD plate. However, no unique slope can be attributed to the Tafel plots at both BDD

299   electrodes due to the complex set of the electrochemical reactions taking place involving

300   most probably the OER and persulfate production. Tafel slopes about 0.6117 V decade^{-1} and

301   0.5363 V decade^{-1} for BDD plate and BDD/B:CNW electrode were estimated, respectively,

302   at lower overpotential region. Meanwhile, 0.3810 V decade^{-1} and 0.3740 V decade^{-1} in the

15

303 high overpotential region were obtained for BDD plate and BDD/B:CNW electrodes,

304 respectively. Two distinct linearity regions can be attributed to the electrochemical reactions

305 on the Nernst layer at BDD surface, associated with the sulfate ions in solution and water

306 discharge, which are transformed to persulfate and hydroxyl radicals ($^\bullet$OH) as well as oxygen,

307 respectively [39,40]. From Tafel plots data as well as the current and potentials (inset of Fig.

308 3), it is possible to infer that an important electrochemical reaction at the lower overpotential

309 region is attained at both diamond electrodes, which could be associated with the specific

310 interaction of sulfate ions with each one of the carbon surfaces [37,40,41].

311 Based on the existing literature [3,4,8], in the case of diamond electrodes, the

312 mechanisms followed depend strongly on (i) extension of the oxidation of SO_4^{2-} ions at the

313 diamond surface, via direct electron transfer, to produce persulfate (Eq. 2), (ii) the production

314 of $^\bullet$OH at anode surface in the reaction cage (Eq. 1), (iii) the interaction of $^\bullet$OH with SO_4^{2-}

315 ions, in the Nernst layer, to favor the production of $SO_4^{-\bullet}$ (principal intermediate) and

316 subsequently, persulfate (Eq. 3), as well as, in some cases, the association between the sp^2-

317 impurities on its surface and the adsorption of SO_4^{2-} ions on these active sites to also form

318 $SO_4^{-\bullet}$ and then, producing persulfate (Eqs. 4 and 5),

319 $$2SO_4^{2-} \rightarrow S_2O_8^{2-} + 2e^- \tag{2}$$

320 $$SO_4^{2-} + {}^\bullet OH \rightarrow SO_4^{-\bullet} + H^+ + e^- \tag{3}$$

321 $$BDD(SO_4^{2-}) \rightarrow BDD(SO_4^{-\bullet}) + e^- \tag{4}$$

322 $$BDD(SO_4^{-\bullet}) + SO_4^{-\bullet} \rightarrow S_2O_8^{2-} \tag{5}$$

323 In the case of the BDD plate, the electrochemical reactions, which occurs at the lower

324 overpotential region (<1.6 V), a more strong interaction is attained than that at BDD/B:CNW.

325   The Tafel slope is higher than the other one (0.6117 V decade^{-1} and 0.5363 V decade^{-1}, for

326   plate BDD and BDD/B:CNW electrode, respectively). These behaviors appear to be

327   associated to the production of $S_2O_8^{2-}$ or $SO_4^{-\bullet}$ at BDD surface [41], evidencing that, a direct

328   electron transfer is attained at BDD plate, in the former. While a fast-adsorptive interaction

329   of SO_4^{2-} ions on B:CNW-active sites (sp^2-configuration) is achieved to form $SO_4^{\bullet-}$ at

330   BDD/B:CNW electrode (Eq. 8) [36]. Afterward, at both electrodes, similar surface-layer-

331   based approaches are accomplished at a higher overpotential region (>1.6 V), which are

332   related to the production of $^\bullet$OH (Eq. 1) and O_2 (Eq. 6) as well as the formation of sulfate-

333   based oxidizing species (such as $SO_4^{-\bullet}$ (Eq. 3) or $S_2O_8^{2-}$ (Eq. 3 and 7)) by the participation

334   of free heterogeneous $^\bullet$OH (Eq. 3).

335    $$2^\bullet OH \rightarrow O_2 + 2H^+ + 2e^- \tag{6}$$

336    $$SO_4^{-\bullet} + SO_4^{2-} \rightarrow S_2O_8^{2-} + e^- \tag{7}$$

337   It is important to remark that, the surface-layer-based processes are achieved closer

338   to the electrode surface, in the Nernst layer (from Armstrong to nanometers), which mainly

339   depend on the diffusion distance of the free heterogeneous $^\bullet$OH, the thickness of the diffusion

340   layer, the convection (agitation and flow rate) and the diffusion coefficient of SO_4^{2-} ions in

341   the solution [8]. However, the limiting steps to produce $S_2O_8^{2-}$ could be regarded as the

342   diffusion of sulfate in the diffusion layer to react with the free heterogeneous $^\bullet$OH (Eq. 3) as

343   well as the subsequent reactions at BDD ($SO_4^{-\bullet}$)-sites on diamond surface (Eq. 5).

344   For this reason, it is necessary to control the current density to stabilize the $S_2O_8^{2-}$

345   electrogenerated, determining the extension of the production of $S_2O_8^{2-}$ at both electrodes.
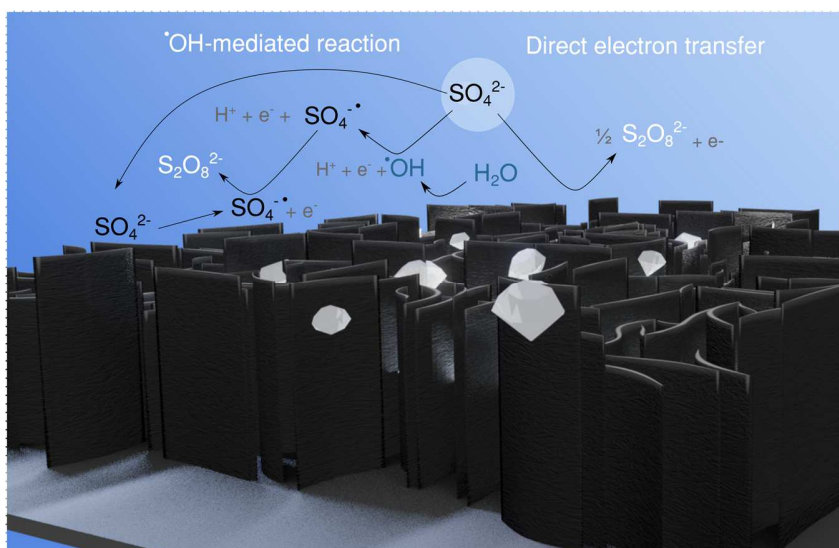
Fig xx – Schematic representation of the persulfate reaction pathway on the BDD/BCNW electrode

3.3. Electrochemical production of persulfate

By applying different current densities (2.5, 5.0 and 15.0 mA cm^{-2}) at 25 °C, the $S_2O_8^{2-}$ concentration produced at both electrodes was determined by ISCO method (Fig. 4). Based on the existing literature, the maximum $S_2O_8^{2-}$ concentration is achieved between 120 and 150 min of electrolysis (inset in Fig. 4), then, the final persulfate concentration was plotted for all electrocatalytic materials at different applied current densities (Figure 4).

18
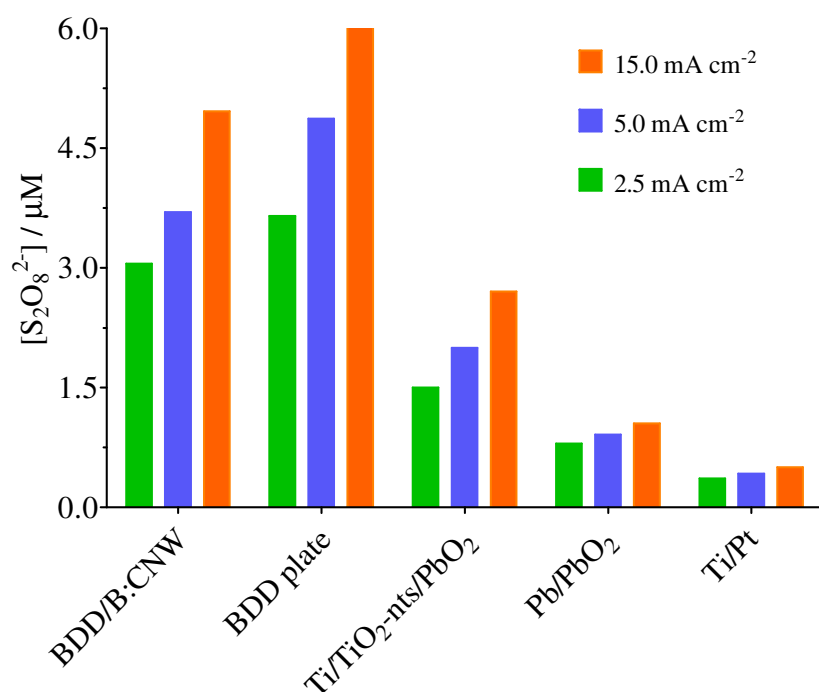
Fig. 4. Electrochemically persulfate generated at different anode materials. Batch cell with 50 mL of 0.05 M Na_2SO_4 at 25°C.

As can be observed, an increase in the concentration of persulfate was attained when the applied current density was increased (Fig. 4). For BDD plate, a significant enhancement in the production of persulfate was attained concerning those achieved at BDD/B:CNW electrode. This behavior is related to the favored mechanism to electrogenerated persulfate [8]. According to the Tafel plot analysis, a stronger interaction is attained at a lower overpotential region (<1.6 V) which indicated that the electrochemical production of $S_2O_8^{2-}$ via direct electron transfer could be attained at BDD plate [3,8]. Meanwhile, at higher potentials, the production of $^{\bullet}OH$ radicals favors an enhancement of the persulfate concentration [29]. Conversely, at BDD/B:CNW anode, the production of persulfate depends

19

368   on the formation of $SO_4^{-\bullet}$ at BDD surface (which seems to be the main intermediate), and the

369   subsequent surface-layer-based reactions of $SO_4^{-\bullet}$ [10,37,42,42]. In this sense, the results

370   related to the quantification of persulfate concentration indicated that the extension of the

371   persulfate mechanism depends on the nature of the electrode and the j (which is directly

372   associated with the cell potential). In fact, at lower j, the increase in the persulfate

373   concentration is less significant than those achieved when higher j. For example, at BDD

374   plate, from 2.5 to 5.0 mA cm^{-2}, the persulfate concentration increases by 1.33-folds, while

375   from 5.0 to 15.0 mA cm^{-2}, it increases by 1.64-folds. Similar behavior is observed at

376   BDD/B:CNW anode, where increases of about 1.21-folds and 1.34-folds were estimated,

377   passing from 2.5 to 5.0 mA cm^{-2}, and from 5.0 to 15.0 mA cm^{-2}, respectively. However, there

378   are significant differences in the persulfate concentrations electrochemically generated.

379   Another feature that should be indicated is that a successive intensification on the j

380   could favor an increase in the production of $^{\bullet}OH$ radicals as well as an increase in the oxygen

381   evolution reaction [43–45]. In the former, these can react with the SO_4^{2-} ions in the diffusion

382   layer to form $SO_4^{-\bullet}$ (Eq. 3); and subsequently, produce $S_2O_8^{2-}$ [42,46]. Meanwhile, when j

383   increases significantly, these can be also wasted favoring the production of O_2 (Eq. 6), in the

384   latter. These assertions are in agreement with the behavior reported by Pires *et al.* using BDD

385   electrode [36], by applying j values higher than 15 mA cm^{-2}. On the contrary, at

386   BDD/B:CNW anode, more active BDD ($SO_4^{-\bullet}$)-sites on the diamond surface can be formed

387   by increasing the j values (Eq. 3), favoring an increase in the production of persulfate via

388   Eqs. (4) and (5).

389   To understand the fundamentals of the mechanism related to the nature of

390   electrocatalytic material, the electrogeneration of persulfate at diamond electrodes was also

391   compared to TiPt, Pb/PbO$_2$ and Ti/TiO$_2$-nanotubes/PbO$_2$. As can be observed at Fig. 4, it is

392   evident that S$_2$O$_8^{2-}$ is efficiently produced at both diamond electrodes, by applying different

393   *j*, with respect to the other anodic materials. This enhancement in the persulfate

394   electrosynthesis is due to the mechanisms associated with the anodic surfaces used as well

395   as the extension of each one of them.

396   Primarily, it is important to remark that no similar production of $^{\bullet}$OH radicals, via

397   water discharge, is attained at all electrocatalytic materials due to their active and non-active

398   nature. Then, following this statement [1,35], higher production of $^{\bullet}$OH radicals implies

399   higher production of persulfate. For example, Ti/Pt produced lower concentrations of S$_2$O$_8^{2-}$

400   (0.36, 0.42 and 0.5 µM at 2.5, 5.0 and 15.0 mA cm^{-2}, respectively) because lower

401   electrogeneration of $^{\bullet}$OH radicals was reached at its surface, limiting the electrosynthesis

402   mechanism via the participation of free heterogeneous $^{\bullet}$OH Eqs. (3), (7) and (8).

403   Conversely, at the diamond electrode (e.g.: BDD plate), the efficient production of

404    $^{\bullet}$OH radicals is attained, favoring the generation of S$_2$O$_8^{2-}$ (such as 3.65, 4.87 and 7.98 µM

405   at 2.5, 5.0 and 15.0 mA cm^{-2}, respectively) via the formation of SO$_4^{-\bullet}$.

406    $$SO_4^{-\bullet} + SO_4^{-\bullet} \rightarrow S_2O_8^{2-} \tag{8}$$

407   Secondly, the formation of S$_2$O$_8^{2-}$ via direct electron transfer and/or via (SO$_4^{-\bullet}$)-active

408   sites on the electrode surfaces depends on the interaction of SO$_4^{2-}$ ions and the

409   electrocatalytic activity of each anode. In this frame, although the extension of the

410   mechanisms is not completely clear, it seems that the electrogeneration of S$_2$O$_8^{2-}$, via direct

411   oxidation of SO$_4^{2-}$, is attained at Ti/Pt surface, as the main approach, confirming that a

412 complex set of electrochemical and chemical reactions can be attained at non-active anodes

413 and consequently, improving the electrosynthesis yield of $S_2O_8^{2-}$ concentration.

414

415 **3.4.   Electrochemical oxidation of a target organic compound**

416 To evaluate the performance of the persulfate electrochemically generated at diamond

417 surfaces and the other materials, oxidation in-situ experiments were carried out. Solutions of

418 25 mL of 0.05 M of Na_2SO_4 containing 10 mg L^{-1} of MO were electrochemically treated by

419 applying 15 mA cm^{-2}, mixing with magnetic stirring during 40 min and aliquots were

420 withdrawn at predetermined times to determine the color removal, COD decay, and the

421 concentration of the target pollutant by an electroanalytic procedure. As can be observed in

422 Fig. 5, EO process with BDD/B:CNW anode removed more than 95% of solution color in 5

423 min of electrolysis. Meanwhile, 93.8%, 95.7%, 98.6% and 85.8% were removed in 7, 10, 15

424 and 25 min at BDD plate, Ti/TiO$_2$-nanotubes/PbO$_2$, Pb/PbO$_2$ and TiPt, respectively.

425 According to the spectrophotometric measurements, the intensity of the visible band at 465

426 nm continuously diminished until it disappears as a function of time during the galvanostatic

427 electrolysis, leading to complete solution discoloration, in all cases. However, the absorbance

428 changes were reasonably rapid at BDD/B:CNW, BDD plate, Ti/TiO$_2$-nanotubes/PbO$_2$ and

429 Pb/PbO$_2$ anodes, indicating that the fragmentation of the MO chromophore group is rapidly

430 attained [29], promoting the elimination of color's solution and after that, the formation of

431 many other intermediates.

22

432
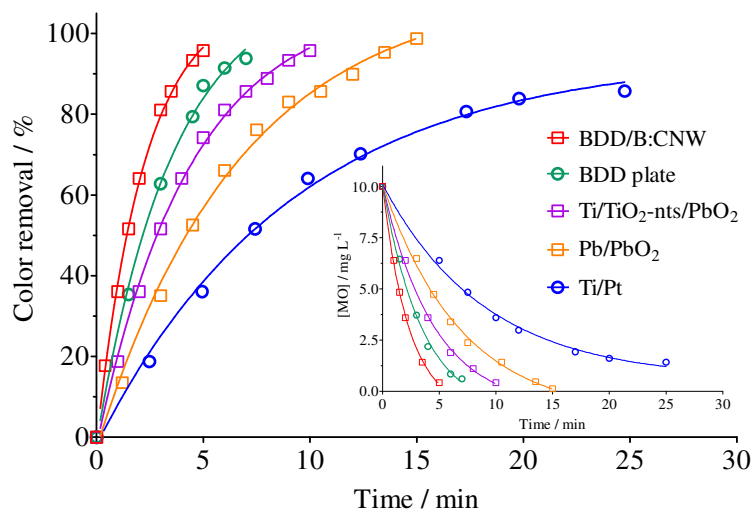
Fig. 5. Color removal effectiveness, as a function of time, at different anodic materials electrogenerating *in-situ* sulfate-based oxidizing species by applying 15 mA cm^{-2} at 25°C. Inset: MO concentration decay, as a function of time, under similar experimental conditions.

In fact, when MO concentration was followed during the EO tests, it gradually decreased and it was dependent on the nature of the material used. Again, non-active anodes were more efficient to remove MO from the solution (inset in Fig. 5), following an efficacy order as BDD/B:CNW>BDD plate>Ti/TiO$_2$-nanotubes/PbO$_2$>Pb/PbO$_2$>Ti/Pt. Only Ti/Pt anode was less efficient, achieving 85% of removal from the MO initial concentration. Analyzing the results obtained, BDD/B:CNW seems to be the most efficient anodic material for the elimination of organic compounds from aqueous solution via SO$_4^{2-}$/SO$_4^{\bullet-}$/S$_2$O$_8^{2-}$ system in concomitance with free heterogeneous $^\bullet$OH. However, the elimination of color and MO is not an indicator of the effective removal of organic matter. Therefore, COD removal was evaluated, at the end of the electrolysis time (40 min), by applying low and high *j* values

23

446 (2.5 and 15 mA cm^{-2}). As observed in Fig. 6, different residual values of COD were

447 determined indicating that the organic matter was oxidized in all cases.
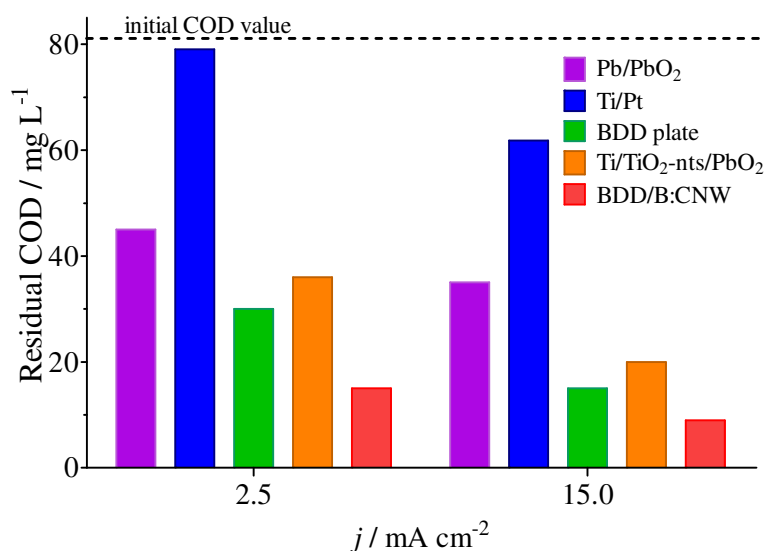
448

449 **Fig. 6.** Residual COD values, as a function of j (2.5 and 15.0 mA cm^{-2}), after 40 min of

450 electrolysis at different anodic materials in EO tests at 25°C.

451

452   On the one hand, residual COD concentrations in solution of about 15.1 and 9.0 mg

453 L^{-1} were determined at 2.5 and 15 mA cm^{-2} with BDD/B:CNW anode corresponding to

454 81.80% and 89.15% of COD removals, considering 83.0 mg L^{-1} as initial COD. On the other

455 hand, lower COD removals (4.76% and 25.51% at 2.5 and 15 mA cm^{-2}, respectively) were

456 achieved using Ti/Pt, as electrocatalytic material, that still represents a significant amount of

457 dissolved organic matter in solution. Based on these results, it is clear that the elimination of

458 organic matter occurred by the reactions attained in the reaction cage as surface-layer-based

459 approaches via $SO_4^{\bullet-}$, $S_2O_8^{2-}$ and free heterogeneous $^\bullet OH$. But, the intensification of the

24

460   process is attained when a synergic effect is reached via the participation of all oxidant

461   species, which depends on the extension of the electrogeneration of each one of the oxidants,

462   mainly at non-active anodes.

463   The results obtained at diamond electrodes, such as the real surface area, Tafel plots,

464   persulfate production, and electrochemical degradation, evidenced that the concentration of

465     $SO_4^{\bullet-}$, $S_2O_8^{2-}$ and free heterogeneous $^{\bullet}OH$ could be different, under the experimental

466   conditions exposed here. This hypothesis is mainly related to the efficacy to produce

467   persulfate, discoloration level, and MO decay as well as COD removal comparing both BDD

468   plate and BDD/B:CNW anodes. In the former, all parameters were efficiently achieved and

469   superior to BDD/B:CNW anode. Meanwhile, COD was significantly removed from synthetic

470   effluent at BDD/B:CNW anode than the other electrodes. This behavior could be associated

471   with the electrochemical generation of prior species that reacts in Nernst layer with the

472   organic compound before generating $S_2O_8^{2-}$. According to the literature [8,29], $SO_4^{-\bullet}$ radicals

473   are the potential candidate, as already experimental [41] and theoretically [47] established;

474   in the case of diamond electrodes, the formation of $BDD\text{-}(SO_4^{\bullet-})$ sites is a pre-requisite step

475   to produce $S_2O_8^{2-}$ by recombining two $SO_4^{\bullet-}$ species (Eq. (13)). However, as already proved

476   by electrochemical measurements, this behavior is strongly dependent on the carbon sp^2-

477   impurities content on the BDD surface. Graphitic sp^2 carbon act as the adsorption site for

478   sulfate-based species (e.g., SO_4^{2-}, HSO_4^-) at the diamond electrode, favoring the generation

479   of $SO_4^{-\bullet}$, thus producing $S_2O_8^{2-}$. In the case of BDD/B:CNW electrode, its surface was

480   meaningly enlarged due to the 3D-diamond-carbon nanostructures. These nanostructures

481   (nano-flaps, nanowalls, as well as microcavities and micro-valleys) contain a key quantity of

482   hot-spot active sites, which could participate as adsorption sulfate-based species.

25

483   3D-diamond-carbon nanostructures + $SO_4^{2-}{}_{(aq)}$ → 3D-diamond-carbon nanostructures-(

484   SO_4^{2-})$_{ads}$ (9)

485   3D-diamond-carbon nanostructures-($SO_4^{-\bullet}$)$_{ads}$ + $SO_4^{-\bullet}$ → $S_2O_8^{2-}$ (10)
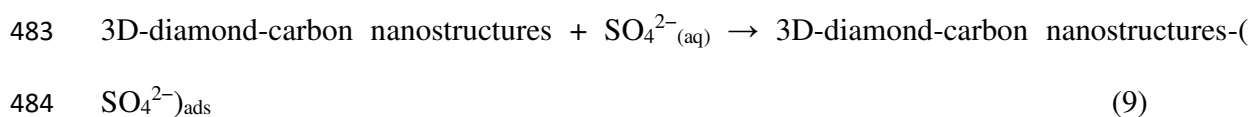
486   In this context, the formation of active-($SO_4^{-\bullet}$) sites is mainly attained at BDD/B:CNW (Eq.

487   9), producing higher concentrations of $SO_4^{-\bullet}$ at its surface when compared to the production

488   of free heterogeneous $^{\bullet}OH$. Although similar oxidation-reduction potentials are registered

489   between $SO_4^{-\bullet}$ (2.5–3.1 V vs. NHE) and $^{\bullet}OH$ (2.74 V vs. NHE), different extinction lifetimes

490   are attained in solution, 30–40 μs for $SO_4^{-\bullet}$ and less than 1 μs for $^{\bullet}OH$ [8], which allows to

491   substantially improve the $SO_4^{-\bullet}$ mass transfer performances and subsequently, its contact

492   chance and effectiveness with the pollutants in solution, as *surface-layer-* or as *volume-*

493   *solution-* oxidation approaches [3,8,9,29,48]. Additionally, a wide pH window (from 2.0 to

494   8.0), due to the pH adjustment, can be used to favor the efficacy of the $SO_4^{-\bullet}$ with the organic

495   pollutants. Consequently, BDD/B:CNW produces a higher concentration of $SO_4^{-\bullet}$ that, which

496   is available at active sites on its surface with a substantial lifetime, enhances the organic

497   matter removal (see Fig. 6) concerning other electrodes, mainly BDD plate.

498

499   **Conclusions**

500   In summary, we can conclude that,

501   (i)   BDD/B:CNW electrode is constituted by 3D-diamond-carbon nanostructures

502   which increase significantly its electroactive surface area, as confirmed by the

503   double layer capacitance determination obtaining an expansion of about 3.2-

504   folds respect to the area of a BDD plate.

26

505   (ii)   The roughness factor indicated that the 3D-nanomaterial increased its porous

506   properties which were also confirmed by SEM images for BDD/B:CNW

507   surface.

508   (iii)   In both diamond materials, electrochemical measurements have indicated that

509   the complex set of the electrochemical reactions takes at lower and higher

510   over potential regions. However, it mainly seems that the persulfate

511   electrosynthesis depends on the stability/reactivity of $^{\bullet}OH$ and diamond

512   surface active sites to favor the production of $SO_4^{-\bullet}$. In the case of BDD plate,

513   it produces rapidly $SO_4^{-\bullet}$, via reaction between $^{\bullet}OH$ and SO_4^{2-}, which form

514                 $S_2O_8^{2-}$, but it is a less reactive oxidizing species. Meanwhile, $SO_4^{-\bullet}$ species

515   are adsorbed at sp2-active sites at BDD/B:CNW favoring their participation

516   in the oxidation of MO.

517   (iv)   In the case of PbO_2-based electrodes, indirect oxidation of SO_4^{2-} via

518   heterogeneous free $^{\bullet}OH$ can be hypnotized where a possible formation of the

519   active-($SO_4^{-\bullet}$) sites can be also feasible at α- PbO_2 or β- PbO_2 sites, which

520   should be still completely elucidated.

521   These conclusions open a new landscape associated with the real mechanism to

522   produce sulfate-based oxidizing species at BDD anodes as well as the electrochemical

523   generation of these oxidants at other non-active and active anodes.

524

525

526

5. References

[1]   C.A. Martínez-Huitle, M. Panizza, Electrochemical oxidation of organic pollutants for wastewater treatment, Curr. Opin. Electrochem. 11 (2018) 62–71. https://doi.org/10.1016/j.coelec.2018.07.010.

[2]   C.A. Martínez-Huitle, M.A. Rodrigo, I. Sirés, O. Scialdone, C.A. Martinez-Huitle, M.A. Rodrigo, I. Sire, O. Scialdone, Single and Coupled Electrochemical Processes and Reactors for the Abatement of Organic Water Pollutants: A Critical Review, Chem. Rev. 115 (2015) 13362–13407. https://doi.org/10.1021/acs.chemrev.5b00361.

[3]   S.O. Ganiyu, C.A. Martínez-Huitle, M.A. Oturan, Electrochemical advanced oxidation processes for wastewater treatment: Advances in formation and detection of reactive species and mechanisms, Curr. Opin. Electrochem. 27 (2021). https://doi.org/10.1016/j.coelec.2020.100678.

[4]   S.O. Ganiyu, E.V. dos Santos, C.A. Martínez-Huitle, S.R. Waldvogel, Opportunities

28

552   and challenges of thin-film boron-doped diamond electrochemistry for valuable

553   resources recovery from waste: Organic, inorganic, and volatile

554   product electrosynthesis, Curr. Opin. Electrochem. (2021) 100903.

555   https://doi.org/10.1016/J.COELEC.2021.100903.

556   [5]   G.R. Salazar-Banda, G.D.O.S. Santos, I.M. Duarte Gonzaga, A.R. Dória, K.I.

557   Barrios Eguiluz, Developments in electrode materials for wastewater treatment,

558   Curr. Opin. Electrochem. 26 (2021). https://doi.org/10.1016/j.coelec.2020.100663.

559   [6]   D. Clematis, M. Panizza, Application of boron-doped diamond electrodes for

560   electrochemical oxidation of real wastewaters, Curr. Opin. Electrochem. (2021)

561   100844. https://doi.org/10.1016/J.COELEC.2021.100844.

562   [7]   P.V. Nidheesh, M. Zhou, M.A. Oturan, An overview on the removal of synthetic

563   dyes from water by electrochemical advanced oxidation processes, Chemosphere.

564   197 (2018) 210–227. https://doi.org/10.1016/j.chemosphere.2017.12.195.

565   [8]   G. Divyapriya, P. V. Nidheesh, Electrochemically generated sulfate radicals by

566   boron doped diamond and its environmental applications, Curr. Opin. Solid State

567   Mater. Sci. 25 (2021) 100921. https://doi.org/10.1016/J.COSSMS.2021.100921.

568   [9]   C.A. Martínez-Huitle, E. Brillas, A critical review over the electrochemical

569   disinfection of bacteria in synthetic and real wastewaters using a boron-doped

570   diamond anode, Curr. Opin. Solid State Mater. Sci. 25 (2021) 100926.

571   https://doi.org/10.1016/j.cossms.2021.100926.

572 [10] K. Groenen Serrano, A critical review on the electrochemical production and use of

573   peroxo-compounds, Curr. Opin. Electrochem. 27 (2021) 100679.

574   https://doi.org/10.1016/j.coelec.2020.100679.

575 [11] A.S. Mora, S.T. McBeath, C.A. Cid, M.R. Hoffmann, N.J.D. Graham, Diamond

576   electrode facilitated electrosynthesis of water and wastewater treatment oxidants,

577   Curr. Opin. Electrochem. 32 (2022) 100899.

578   https://doi.org/10.1016/J.COELEC.2021.100899.

579 [12] G.R. Pointer Malpass, A. de Jesus Motheo, Recent advances on the use of active

580   anodes in environmental electrochemistry, Curr. Opin. Electrochem. (2021) 100689.

581   https://doi.org/10.1016/j.coelec.2021.100689.

582 [13] X. Du, M.A. Oturan, M. Zhou, N. Belkessa, P. Su, J. Cai, C. Trellu, E. Mousset,

583   Nanostructured electrodes for electrocatalytic advanced oxidation processes: From

584   materials preparation to mechanisms understanding and wastewater treatment

585   applications, Appl. Catal. B Environ. 296 (2021) 120332.

586   https://doi.org/10.1016/J.APCATB.2021.120332.

587 [14] M. Pierpaoli, P. Jakobczyk, M. Sawczak, A. Łuczkiewicz, S. Fudala-Książek, R.

588   Bogdanowicz, Carbon nanoarchitectures as high-performance electrodes for the

589   electrochemical oxidation of landfill leachate, J. Hazard. Mater. 401 (2021) 123407.

590   https://doi.org/10.1016/J.JHAZMAT.2020.123407.

591 [15] M. Pierpaoli, M. Szopińska, B.K. Wilk, M. Sobaszek, A. Łuczkiewicz, R.

592   Bogdanowicz, S. Fudala-Książek, Electrochemical oxidation of PFOA and PFOS in

593   landfill leachates at low and highly boron-doped diamond electrodes, J. Hazard.

594   Mater. 403 (2021). https://doi.org/10.1016/j.jhazmat.2020.123606.

595 [16] S. Dutta, A. Bhaumik, K.C.W. Wu, Hierarchically porous carbon derived from

596   polymers and biomass: effect of interconnected pores on energy applications, Energy

597   Environ. Sci. 7 (2014) 3574–3592. https://doi.org/10.1039/C4EE01075B.

598 [17] B.K. Mishra, S. Chakraborty, P. Kumar, C. Saraswat, Sustainable Solutions for

599   Urban Water Security, 93 (2020). https://doi.org/10.1007/978-3-030-53110-2.

[18]   B. Van der Bruggen, Sustainable implementation of innovative technologies for water purification, Nat. Rev. Chem. 2021 54. 5 (2021) 217–218. https://doi.org/10.1038/s41570-021-00264-7.

[19]   M. Pierpaoli, A. Dettlaff, M. Szopińska, K. Karpienko, M. Wróbel, A. Łuczkiewicz, S. Fudala-Książek, R. Bogdanowicz, Simultaneous opto-electrochemical monitoring of carbamazepine and its electro-oxidation by-products in wastewater, J. Hazard. Mater. 419 (2021). https://doi.org/10.1016/j.jhazmat.2021.126509.

[20]   R. Bogdanowicz, Functionalized nanodiamonds as a perspective green carbo-catalyst for removal of emerging organic pollutants, Curr. Opin. Solid State Mater. Sci. 26 (2022) 100991. https://doi.org/10.1016/J.COSSMS.2022.100991.

[21]   R. Bogdanowicz, J. Ryl, Structural and electrochemical heterogeneities of boron-doped diamond surfaces, Curr. Opin. Electrochem. 31 (2022) 100876. https://doi.org/10.1016/J.COELEC.2021.100876.

[22]   K. Siuzdak, M. Ficek, M. Sobaszek, J. Ryl, M. Gnyba, P. Niedziałkowski, N. Malinowska, J. Karczewski, R. Bogdanowicz, Boron-Enhanced Growth of Micron-Scale Carbon-Based Nanowalls: A Route toward High Rates of Electrochemical Biosensing, ACS Appl. Mater. Interfaces. 9 (2017) 12982–12992. https://doi.org/10.1021/ACSAMI.6B16860/SUPPL_FILE/AM6B16860_SI_001.PDF.

[23]   A. Dettlaff, P. Jakóbczyk, M. Ficek, B. Wilk, M. Szala, J. Wojtas, T. Ossowski, R. Bogdanowicz, Electrochemical determination of nitroaromatic explosives at boron-doped diamond/graphene nanowall electrodes: 2,4,6-trinitrotoluene and 2,4,6-trinitroanisole in liquid effluents, J. Hazard. Mater. 387 (2020) 121672. https://doi.org/10.1016/J.JHAZMAT.2019.121672.

624　　[24]　M. Sobaszek, K. Siuzdak, J. Ryl, M. Sawczak, S. Gupta, S.B. Carrizosa, M. Ficek,

625　　　　　B. Dec, K. Darowicki, R. Bogdanowicz, Diamond Phase (sp3-C) Rich Boron-Doped

626　　　　　Carbon Nanowalls (sp2-C): Physicochemical and Electrochemical Properties, J.

627　　　　　Phys. Chem. C. 121 (2017) 20821–20833.

628　　　　　https://doi.org/10.1021/ACS.JPCC.7B06365/ASSET/IMAGES/MEDIUM/JP-2017-

629　　　　　063658_0016.GIF.

630　　[25]　S. Trasatti, Electrocatalysis: understanding the success of DSA®, Electrochim. Acta.

631　　　　　45 (2000) 2377–2385. https://doi.org/10.1016/S0013-4686(00)00338-8.

632　　[26]　C. Calas-Blanchard, M. Comtat, J.L. Marty, S. Mauran, Textural characterisation of

633　　　　　graphite matrices using electrochemical methods, Carbon N. Y. 41 (2003) 123–130.

634　　　　　https://doi.org/10.1016/S0008-6223(02)00269-5.

635　　[27]　M. Łukaszewski, Electrochemical Methods of Real Surface Area Determination of

636　　　　　Noble Metal Electrodes – an Overview, Int. J. Electrochem. Sci. 11 (2016) 4442–

637　　　　　4469. https://doi.org/10.20964/2016.06.71.

638　　[28]　C. Liang, C.F. Huang, N. Mohanty, R.M. Kurakalva, A rapid spectrophotometric

639　　　　　determination of persulfate anion in ISCO, Chemosphere. 73 (2008) 1540–1543.

640　　　　　https://doi.org/10.1016/j.chemosphere.2008.08.043.

641　　[29]　K.C.F. Araújo, K.N.O. Silva, M.K.S. Monteiro, D.R. da Silva, M.A. Quiroz, E.V.

642　　　　　dos Santos, C.A. Martínez-Huitle, Towards Use of Persulfate Electrogenerated at

643　　　　　Boron Doped Diamond Electrodes as Ex-Situ Oxidation Approach: Storage and

644　　　　　Service-Life Solution Parameters, J. Electrochem. Soc. 169 (2022) 033506.

645　　　　　https://doi.org/10.1149/1945-7111/AC59F8.

646　　[30]　G.O.S. Santos, K.I.B. Eguiluz, G.R. Salazar-Banda, C. Sáez, M.A. Rodrigo,

647　　　　　Understanding the electrolytic generation of sulfate and chlorine oxidative species

648   with different boron-doped diamond anodes, J. Electroanal. Chem. 857 (2020)

649   113756. https://doi.org/10.1016/j.jelechem.2019.113756.

650 [31] H. Huang, M. Yan, C. Yang, H. He, Q. Jiang, L. Yang, Z. Lu, Z. Sun, X. Xu, Y.

651   Bando, Y. Yamauchi, Graphene Nanoarchitectonics: Recent Advances in Graphene-

652   Based Electrocatalysts for Hydrogen Evolution Reaction, Adv. Mater. 31 (2019)

653   1903415. https://doi.org/10.1002/ADMA.201903415.

654 [32] O.A. Trasatti, S, Petri, Real surface area measurements in electrochemistry, J.

655   Electroanal. Chem. 327 (1992) 353–376.

656   https://doi.org/https://doi.org/10.1016/0022-0728(92)80162-W.

657 [33] J.M. Doña Rodríguez, J.A. Herrera Melián, J. Pérez Peña, Determination of the Real

658   Surface Area of Pt Electrodes by Hydrogen Adsorption Using Cyclic Voltammetry,

659   J. Chem. Educ. 77 (2000) 1195. https://doi.org/10.1021/ed077p1195.

660 [34] R. Bogdanowicz, A. Fabiańska, L. Golunski, M. Sobaszek, M. Gnyba, J. Ryl, K.

661   Darowicki, T. Ossowski, S.D. Janssens, K. Haenen, E.M. Siedlecka, Influence of the

662   boron doping level on the electrochemical oxidation of the azo dyes at Si/BDD thin

663   film electrodes, Diam. Relat. Mater. 39 (2013) 82–88.

664   https://doi.org/https://doi.org/10.1016/j.diamond.2013.08.004.

665 [35] J. Ryl, L. Burczyk, A. Zielinski, M. Ficek, A. Franczak, R. Bogdanowicz, K.

666   Darowicki, Heterogeneous oxidation of highly boron-doped diamond electrodes and

667   its influence on the surface distribution of electrochemical activity, Electrochim.

668   Acta. 297 (2019) 1018–1027. https://doi.org/10.1016/J.ELECTACTA.2018.12.050.

669 [36] J.P. De Paiva Barreto, K.C. De Freitas Aráujo, D.M. De Aráujo, C.A. Martínez-

670   Huitle, Effect of sp3/sp2 ratio on boron doped diamond films for producing

671   persulfate, ECS Electrochem. Lett. 4 (2015) E9–E11.

672   https://doi.org/10.1149/2.0061512eel.

673 [37] T.F. Da Costa, J.E.L. Santos, D.R. da Silva, C.A. Martinez-Huitle, BDD-electrolysis

674   of oxalic acid in diluted acidic solutions, J. Braz. Chem. Soc. 30 (2019) 1541–1547.

675   https://doi.org/10.21577/0103-5053.20190051.

676 [38] P.K. Jiwanti, K. Natsui, K. Nakata, Y. Einaga, The electrochemical production of

677   C2/C3 species from carbon dioxide on copper-modified boron-doped diamond

678   electrodes, Electrochim. Acta. 266 (2018) 414–419.

679   https://doi.org/10.1016/j.electacta.2018.02.041.

680 [39] P.A. Michaud, M. Panizza, L. Ouattara, T. Diaco, G. Foti, C. Comninellis,

681   Electrochemical oxidation of water on synthetic boron-doped diamond thin film

682   anodes, J. Appl. Electrochem. 33 (2003) 151–154.

683   https://doi.org/10.1023/A:1024084924058.

684 [40] K. Serrano, P.A. Michaud, C. Comninellis, A. Savall, Electrochemical preparation of

685   peroxodisulfuric acid using boron doped diamond thin film electrodes, Electrochim.

686   Acta. 48 (2002) 431–436. https://doi.org/https://doi.org/10.1016/S0013-

687   4686(02)00688-6.

688 [41] K.C. de Freitas Araújo, D.R. da Silva, E.V. dos Santos, H. Varela, C.A. Martínez-

689   Huitle, Investigation of persulfate production on BDD anode by understanding the

690   impact of water concentration, J. Electroanal. Chem. 860 (2020) 113927.

691   https://doi.org/10.1016/j.jelechem.2020.113927.

692 [42] Y.U. Shin, H.Y. Yoo, Y.Y. Ahn, M.S. Kim, K. Lee, S. Yu, C. Lee, K. Cho, H. il

693   Kim, J. Lee, Electrochemical oxidation of organics in sulfate solutions on boron-

694   doped diamond electrode: Multiple pathways for sulfate radical generation, Appl.

695   Catal. B Environ. 254 (2019) 156–165.

696   https://doi.org/10.1016/J.APCATB.2019.04.060.

697   [43]   W. Wu, Z.H. Huang, T.T. Lim, Recent development of mixed metal oxide anodes

698   for electrochemical oxidation of organic pollutants in water, Appl. Catal. A Gen. 480

699   (2014) 58–78. https://doi.org/10.1016/J.APCATA.2014.04.035.

700   [44]   M.S.M. Sillanpää, Electrode materials used for electrochemical oxidation of organic

701   compounds in wastewater, (n.d.). https://doi.org/10.1007/s11157-017-9426-1.

702   [45]   M. Moradi, Y. Vasseghian, A. Khataee, M. Kobya, H. Arabzade, E.N. Dragoi,

703   Service life and stability of electrodes applied in electrochemical advanced oxidation

704   processes: A comprehensive review, J. Ind. Eng. Chem. 87 (2020) 18–39.

705   https://doi.org/10.1016/J.JIEC.2020.03.038.

706   [46]   L.W. Matzek, M.J. Tipton, A.T. Farmer, A.D. Steen, K.E. Carter, Understanding

707   Electrochemically Activated Persulfate and Its Application to Ciprofloxacin

708   Abatement, Environ. Sci. Technol. 52 (2018) 5875–5883.

709   https://doi.org/10.1021/ACS.EST.8B00015/SUPPL_FILE/ES8B00015_SI_001.PDF.

710   [47]   J. Davis, J.C. Baygents, J. Farrell, Understanding Persulfate Production at Boron

711   Doped Diamond Film Anodes, Electrochim. Acta. 150 (2014) 68–74.

712   https://doi.org/10.1016/j.electacta.2014.10.104.

713   [48]   K.N.O. Silva, K.C.F. Araújo, D.R. da Silva, C.A. Martínez-Huitle, E.V. dos Santos,

714   Persulfate-soil washing: The green use of persulfate electrochemically generated

715   with diamond electrodes for depolluting soils, J. Electroanal. Chem. 895 (2021)

716   115498. https://doi.org/10.1016/j.jelechem.2021.115498.

717